Research article

Yeon Ui Lee, Igor Ozerov, Frédéric Bedu, Ji Su Kim, Frédéric Fages and Jeong Weon Wu*

Optical spin-dependent beam separation in cyclic group symmetric metasurface

https://doi.org/10.1515/nanoph-2020-0160
Received March 1, 2020; accepted April 30, 2020

Abstract: Cross-polarization scattering of a circularly polarized beam from nano-rod introduces a geometric phase to the outgoing beam with opposite circular polarization. By manipulating the spatial array of subwavelength nano-structure constituting metasurface, the geometric phase can be engineered to generate a variety of beam profiles, including vortex beam carrying orbital angular momentum via a process called spin-to-orbital angular momentum conversion. Here we introduce a cyclic group symmetric metasurface composed of tapered arc nano-rods and explore how azimuthal angular distribution of total phase determines the feature of spin-dependent beam separation. When scattered from a circular array of tapered arc nano-rods possessing varying width with a fixed length, a dynamical phase having non-constant azimuthal gradient is introduced to an incoming Gaussian beam. This leads to a spin-dependent beam separation in the outgoing vortex beam profile, which is attributed to an azimuthal angle dependent destructive interference between scatterings from two plasmonic excitations along the width and the length of tapered arc nano-rod. Relation of cyclic group symmetry property of metasurface and the generated vortex beam profile is examined in detail by experimental measurement and analysis in terms of partial-wave expansion and non-constant azimuthal gradient of total phase. Capability of spatial beam profiling by spin-dependent beam separation in vortex beam generation has an important implication for spatial demultiplexing in optical communication utilizing optical angular momentum mode division multiplexing as well as for optical vortex tweezers and optical signal processing employing vortex beams.

Keywords: cyclic group symmetric metasurface; metamaterial; optical spin; vortex beam.

Current address: Yeon Ui Lee, Department of Electrical and Computer Engineering, University of California, San Diego, La Jolla, CA 92093, USA

***Corresponding author: Jeong Weon Wu**, Department of Physics, Ewha Womans University, Seoul, 03760, Republic of Korea, E-mail: jwwu@ewha.ac.kr
Yeon Ui Lee and Ji Su Kim: Department of Physics, Ewha Womans University, Seoul, 03760, Republic of Korea, E-mail: yeonuilee@ewhain.net (Y.U. Lee), jisuorange@naver.com (J.S. Kim). https://orcid.org/0000-0001-8857-1251 (Y.U. Lee)
Igor Ozerov, Frédéric Bedu and Frédéric Fages: Aix-Marseille Univ, CNRS, CINaM UMR 7325, Marseille, France, E-mail: ozerov@cinam.univ-mrs.fr (I. Ozerov), bedu@cinam.nuiv-mrs.fr (F. Bedu), fages@cinam.univ-mrs.fr (F. Fages). https://orcid.org/0000-0001-5839-7854 (I. Ozerov) . https://orcid.org/0000-0003-2013-0710 (F. Fages)

Novelty and impact statement

Vortex beam generation by geometric phase is known. However, a systematic study of relating symmetry property of cyclic group C_{nh} and vortex beam profile is never reported. This work shows that non-constant azimuthal gradient of total phase is the key in controlling azimuthal interference pattern of vortex beam with asymmetric helical wavefront. Noting the importance of vortex beam communications, this work opens a novel way to manipulate interplay between spin- and orbital angular momentum for vortex beam profiling.

1 Introduction

Since the pioneering work of Hasman group on Pancharatnam-Berry (PB) phase to manipulate wavefront of optical beam, [1–5] application of geometric phase has been expanded to metasufrace to open a research field of flat optics. [6–10] PB phase is a geometric phase, associated not with optical path but with polarization, which can be utilized for beam deflection or vortex beam generation, when a cross-polarization scattering of circular polarized light (CPL) takes place in an array of sub-wavelength nano-rods. [1–3]

Regrading a helical wavefront formation, a circular array of sub-wavelength scatterers introduces a geometric phase linearly increasing along azimuthal direction, allowing spin-to-orbital angular momentum conversion to generate a vortex beam possessing topological charge. Examples include metal nano-rods patterned from computer-generated holograms, [3] liquid crystal q-plate, [11,

Open Access. © 2020 Yeon Ui Lee et al., published by De Gruyter. This work is licensed under the Creative Commons Attribution 4.0 Public License.

12] uniaxial crystal, [13] nano-slits, [14] spatial light modulator, [15] plasmonic metasurface, [16, 17] V-shaped antenna array, [18], bulls-eye plasmon antennas, [19] TiO_2 nanostructures, [20] dielectric metasurface, [21], and ultra-thin metalenses [22].

Metallic nano-rod is of a rectangular shape having two principal axes of plasmonic excitations along the width and the length. When nano-rods of the same rectangular shape are arrayed head-to-tail in a circle, the geometric phase $\Phi_{PB}(\phi)$ introduced by two neighboring nano-rods increases linearly along azimuthal direction, leading to a helical wavefront formation to generate a vortex beam of topological charge ±2. By arranging the rotation angle of each nano-rod of circular array in a specific way, vortex beams of arbitrary topological charges can be generated [17].

Let's consider a series of metallic nano-rods possessing varying width with a fixed length. Now, in contrast to the same plasmonic excitation along long-axis of the fixed length, plasmonic excitation along short-axis of varying width is not the same among nano-rods. When the series of metallic nano-rods are arrayed head-to-tail in a circle, the dynamical phase introduced by two neighboring nano-rods of different widths does not increase linearly along azimuthal direction. That is, the azimuthal gradient of dynamical phase $\nabla_\phi\Phi_D(\phi)$which is not a constant of ±2 but depends on the azimuthal angle ϕ. We decompose the total phase $\Phi_{tot}(\phi)$ as a sum of constant and non-constant azimuthal gradient terms, $\Phi_{tot} = \Phi_{PB} + \Phi_D$ with $\nabla_\phi\Phi_{PB} = \pm 2$.

There are several ways to relate the feature of a spin-dependent beam separation in vortex beam generation with the presence of a non-constant azimuthal gradient of total phase $\nabla_\phi\Phi_{tot}$, which is the main topic of this work. First, a partial-wave expansion of cross-polarization scattering amplitude in terms of vortex beams of different topological charge can be adopted to examine the interference between vortex beams. Second, the role of non-constant azimuthal gradient $\nabla_\phi\Phi_{tot}$ can be identified in providing an azimuthal shift of beam to result in a spin-dependent beam separation.

For a systematic study, we introduce nano-structure of tapered arc (TA) having varying width with a fixed length as a unit. Different sizes of TA are arrayed in a circle to obtain metasurface belonging to a cyclic group of C_{nh}, which is named as tapered arc cyclic group symmetric metasurface (TA-CGSM).

Note that in the cyclic group theory, C_{nh} denotes groups containing a horizontal (h) reflection plane, σ_h, in addition to the rotation axis, C_n. That is, C_{nh} refers to a cyclic group with n-fold rotational symmetry by an angle of $360°/n$ and horizontal (h) reflection symmetry in three dimensions. Experimental measurement of vortex beam profiles from cross-polarization scattering of CPL beam from C_{nh} TA-CGSM is carried out and a detailed analysis is presented to relate cyclic group symmetry property of metasurface and the generated vortex beam profile.

First of all, PB phase is examined in Poincaré sphere when cross-polarization scattering takes place from linear and circular arrays of nano-rods with uniform thickness in Section 2. We extend the study of PB phase to the example of circular array of nano-rods with non-uniform thickness in Section 3. Sample fabrication of C_{nh} TA-CGSM and spin-dependent beam profile measurement are presented in Section 4 including elucidation of symmetry properties of C_{nh}. In Section 5 we discuss spin-dependent beam separation in terms of partial-wave expansion, azimuthal interference, and a non-constant azimuthal gradient of total phase $\nabla_\phi\Phi_{tot}$. Also wavelength dispersion of spin-dependent beam separation of vortex beam is discussed in terms of photonic spin Hall effect.

2 PB phase from linear and circular arrays of nano-rods with uniform thickness

We compare linear and circular arrays of eight sub-wavelength nano-rods in providing PB phase through cross-polarization scattering of CPL Gaussian beam. Eight nano-rods rotated in the xy-plane by an angle φ with respect to the neighboring one are schematically shown in Figure 1 (a) and (b) and inset. In Figure 1 (c) PB phase is illustrated in Poincaré sphere, where colored circles correspond to each nano-rod rotated by an angle φ providing a geometric PB phase of 2φ with phase factor of $e^{+i2\phi}$ ($e^{-i2\phi}$) for LCP $\sigma+$(RCP $\sigma-$) incidence beam [2, 3].

In the linear array, a constant PB phase gradient leads to a beam deflection in cross-polarized scattering. The array of nano-rods with uniform thickness provide a constant linear gradient with opposite signs for the left and the right polarized light, deflecting the corresponding beams in opposite directions as Figure 1 (d) and (e).

In the circular array, on the other hand, a constant PB phase gradient takes place in azimuthal direction ϕ providing a spiral phase shift. [23] Importantly, as shown in Figure 1 (c), the polarization states in Poincaré sphere go through a circular trajectory twice providing the solid angle of $\pm 8\pi$, which corresponds to geometric phase of $\pm 4\pi$, generating vortex beam of topological charge $l = \pm 2$, as shown in Figure 1 (f) and (g).

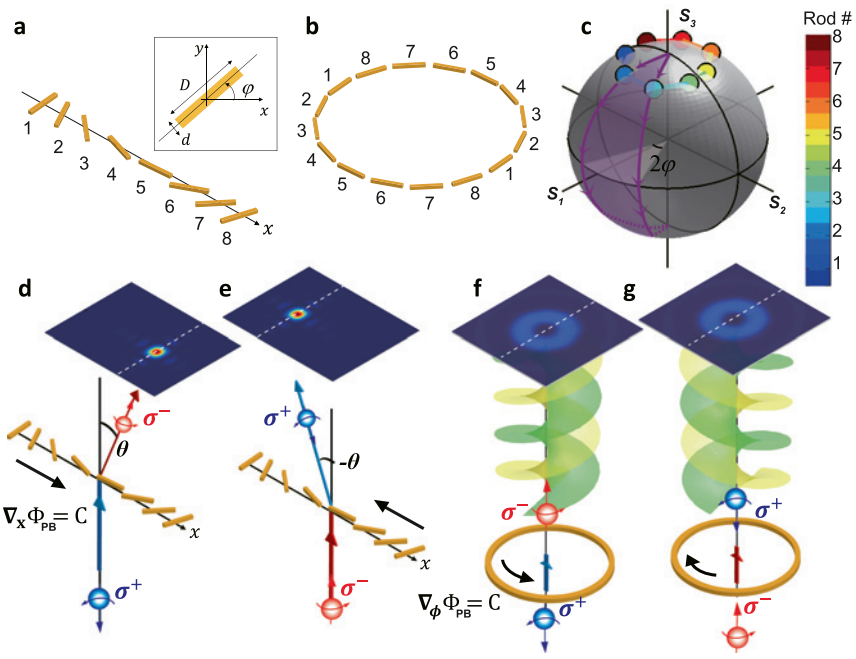


Figure 1: Array of nano-rods with a constant gradient PB phase and Poincaré sphere plot of Stokes parameters. Inset figure shows a schematic of nano-rod with length D and width d making an angle ϕ with x-axis. (a) Linear array of rotating nano-rods from one to eight. (b) Circular array of nano-rods from one to eight in the range of $0 \le \varphi \le \pi$ and repeated in the range of $\pi \le \varphi \le 2\pi$. (c) Poincaré sphere plot of Stokes parameters of optical beams scattered from nano-rods of (a) and (b) for LCP incident beam. Color code corresponds to the nano-rod number. (d,e) Spin-dependent beam deflection of cross-polarization scattered optical beam shown up as a spin-dependent beam separation. +x-direction deflection of RCP $\sigma-$ beam for LCP $\sigma+$ incidence beam in (d) and wereas the opposite in (e). (f, g) Generation of vortex beam of topological charge $l = \pm 2$. Topological charge $l = +2$ with polarization state of RCP $\sigma-$ for LCP $\sigma+$ Gaussian incidence beam in (f), and topological charge $l = -2$ with polarization state of LCP $\sigma+$ for RCP $\sigma-$ Gaussian incidence beam in (g).

Optical wave scattered from the circular array acquires the geometric phase factor coming from a circular closed path C in Poincaré sphere Stokes parameter space, $\oint d\gamma(C) = \pm 4\pi$ with a constant azimuthal gradient $\nabla_\phi \Phi_{PB} = \pm 2$. The intensity profiles of $I_{-+}(r, \phi) = |E_{-+}|^2$ and $I_{+-}(r, \phi) = |E_{+-}|^2$ are degenerate even though helical handedness is opposite for $l = \pm 2$, where $\{+-\} = \{\text{out}, \text{in}\}$ stands for left-circular polarization (LCP, $\sigma+$) scattering/right-circular polarization (RCP, $\sigma-$) incidence and $\{-+\}$ vice-versa. In fact, $E_{-+}(r, \phi) = J_2(k_0 r)\exp(-k_0^2 r^2 + i2\phi)$ and $E_{+-}(r, \phi) = J_{-2}(k_0 r)\exp(-k_0^2 r^2 - i2\phi)$ with nth order Bessel function $J_n(k_0 r)$.

Owing to the rotational invariance of circular array of nano-rods belonging to the cyclic group $C_{\infty h}$, the azimuthal gradient $\nabla_\phi \Phi_{PB}$ is constant, and PB phase is accumulated in sequence by an equal amount originating from two neighboring nano-rods during one full cycle, leading to a ϕ-independent scattered electric field $J_{\pm 2}(r)\exp(-k_0^2 r^2)$.

3 Total phase from circular arrays of nano-rods with non-uniform thickness

Cross-polarization scattering amplitude is determined by optical response of plasmonic resonance of a nano-rod, which depends on oscillator strength and resonance frequency of the nano-rod. Let's consider a nano-rod of length D and width d. See the inset of Figure 1 (a). Upon incidence of an optical beam, there occur plasmonic excitations along two principal axes, i. e., along both long- and short-axis.

When the long-axis is rotated by an angle of φ with respect to x-axis, the short-axis makes an angle of $\theta = \varphi + \frac{\pi}{2}$. This leads to phase factors of $e^{+i2\varphi}$ and $e^{+i2\theta} = -e^{+i2\varphi}$ for cross-polarization scatterings from the long- and short-axis excitations, respectively. Note that phases of 2φ are the same, while the scattering amplitudes are opposite in sign. Refer to (5) in Ref. [23]. In other words, there occurs a destructive interference between scatterings from the long- and short-axis excitations, introducing the same amount of geometric phase of 2φ.

Now we introduce a circular array of nano-rods with varying width d from # 1 to # 16 having a fixed length D, which belongs to the cyclic group C_{1h}, as displayed in Figure 2 (a). Scattering amplitude from the long-axis is the same for nano-rods from # 1 to # 16. As the width d increases from # 1 to # 16, however, scattering amplitude from the short-axis excitation increases owing to larger oscillator strength and the plasmonic resonance closer to the optical wave frequency. The amount of a destructive interference increases between long- and short-axis scatterings, leading to asymmetric total cross-polarization scattering amplitude as the width d increases from # 1 to # 16 along azimuthal angle ϕ direction.

Polarization states of cross-polarization scattering are plotted on Poincaré sphere in Figure 2 (b). Solid angle subtended by two meridians of cross-polarization scatterings from two neighboring nano-rods with different widths d is not a constant but depends on azimuthal angular location ϕ of nano-rod, resulting in a spiral trajectory of polarization states from near the north-pole down to near the equator. This leads to Φ_{tot} possessing a non-constant azimuthal gradient. That is, $\nabla_\phi \Phi_{tot}(\phi)$ depends on the azimuthal angle ϕ, and we can decompose the total phase $\Phi_{tot}(\phi)$ as a sum of constant and non-constant azimuthal gradient terms,

$$\Phi_{tot}(\phi) = \Phi_{PB}(\phi) + \Phi_D(\phi). \quad (1)$$

with $\Phi_{PB}(\phi)$ possessing a constant azimuthal gradient $\nabla_\phi \Phi_{PB}(\phi) = \pm 2$. Here we note that the presence of a non-constant azimuthal gradient term $\Phi_D(\phi)$ originates from ϕ-dependent width of TA plasmonic nanostructures, as discussed above.

Azimuthal angular feature of vortex beam profiles $I_{-+}(r, \phi)$ and $I_{+-}(r, \phi)$ is determined by ϕ-dependence of $\Phi_{tot}(\phi)$. Circular array in Figure 2 (a) belongs to the cyclic group C_{1h}. From the viewpoint of symmetry property, the lowering of rotational symmetry from $C_{\infty h}$ to C_{1h} leads to non-vanishing of Φ_D. As a result, asymmetric helical wavefront is formed and spin-dependent separation takes place with asymmetric vortex beam profile. Bight and dark spots are separated along x-direction for both LCP $\sigma+$ and RCP $(\sigma-)$ Gaussian incidence beams as displayed in Figure 2 (c) and (d). The reason why the separation takes place along x-direction will be discussed in terms of the magnitude of azimuthal gradient $\nabla_\phi \Phi_{tot}(\phi)$ in Section 5.

4 Total phase from circular array of nano-rods with rotational symmetry of cyclic group C_{nh}

Now we introduce metasurface composed of circular array of TAs, which belong to a well-defined cyclic group C_{nh} to study the relationship between cyclic group symmetry property of metasurface and the generated vortex beam profile. Schematics of six different tapered arc cyclic group symmetric metasurfaces (TA-CGSM) are shown in Figure 3 (a).

4.1 Symmetry properties of cyclic group C_{nh}

We note that there exits an important difference between C_{nh} of even and odd numbers of group order n with respect to reflection σ_h, inversion i, and C_2 (π-rotation around z-axis) operation elements. While σ_h is an element of both C_{nh} (even n) and C_{nh} (odd n), i and C_2 are elements of C_{nh} (even n), not of C_{nh} (odd n). Furthermore, for C_{nh} (even n), the product of σ_h and i elements is equal to C_2 element, i. e., $\sigma_h \cdot i = i \cdot \sigma_h = C_2$.

In terms of these symmetry properties of cyclic group C_{nh}, two important features of cross-polarization scattering beam profiles will be discussed. First, σ_h element of C_{nh} is responsible for rotational symmetry property of the intensity profiles of $I_{-+}(r, \phi)$ and $I_{+-}(r, \phi)$ in C_{nh} (both even and odd n) TA-CGSMs. Second, the intensity difference $\Delta I \equiv I_{-+} - I_{+-}$ depends on the relation between $E_{-+}(\phi)$ and $E_{+-}(\phi)$ as well as $\Phi_{tot}^{-+}(\phi)$ and $\Phi_{tot}^{+-}(\phi)$ in C_{nh} (even n) TA-CGSMs, which is dictated by σ_h, i, and C_2 elements of C_{nh} (even n).

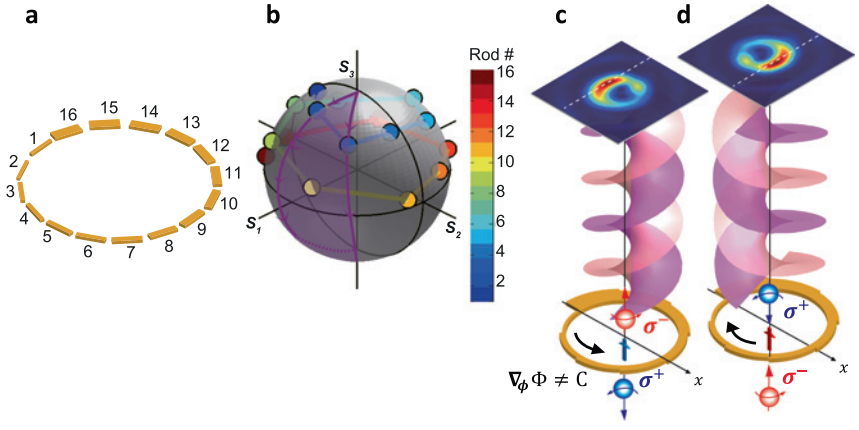


Figure 2: Circular array of nano-rods with a non-constant azimuthal gradient total phase and Poincaré sphere plot of Stokes parameters. (a) Circular array of nano-rods with varying width d from # 1 to # 16 in the range of $0 \le \varphi \le 2\pi$ (b) Poincaré sphere plot of Stokes parameters of optical beams cross-polarization scattered from nano-rods of (a) for LCP $\sigma+$ incidence beam. Color code corresponds to the nano-rod number. (c,d) Generation of asymmetric vortex beam and spin-dependent beam separation. Bight and dark spots are separated along x-direction for both LCP $\sigma+$ in (c) and RCP $(\sigma-)$ in (d) Gaussian incidence beams.

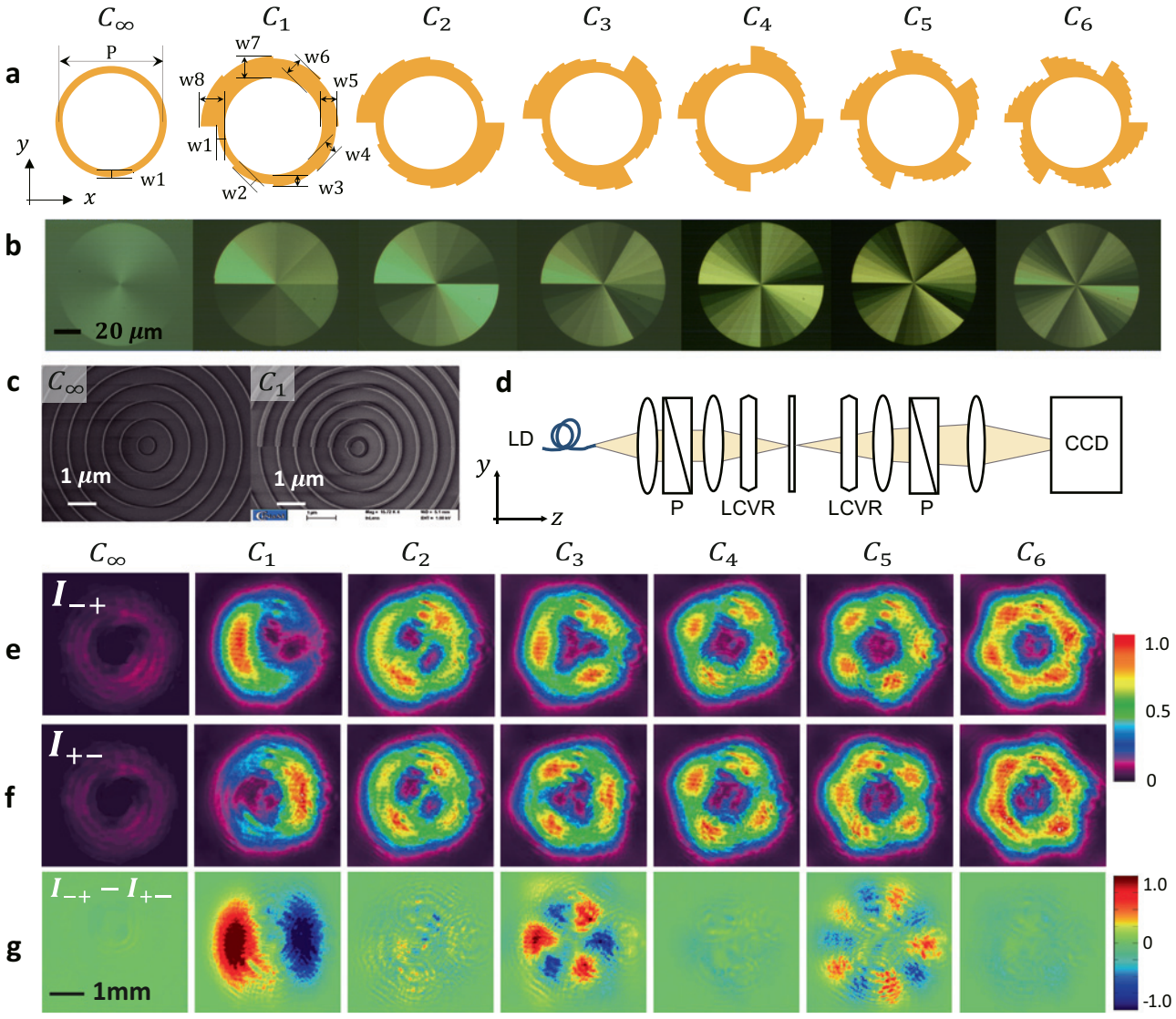


Figure 3: Cyclic group symmetric metasurfaces and a spin- dependent beam separation. (a) Designed TA-CGSM belonging to cyclic groups of $C_{\infty h}$, C_{1h}, C_{2h}, C_{3h}, C_{4h}, C_{5h}, and C_{6h}, respectively. Periodicity is denoted by p = 600 nm, and widths of arcs are by $w1$ = 45 nm, $w2$ = 60 nm, $w3$ = 75 nm, $w4$ = 90 nm, $w5$ = 105 nm, $w6$ = 120 nm, $w7$ = 135 nm, and $w8$ = 150 nm. (b) Optical microscope images of fabricated TA-CGSMs belonging to belonging to cyclic groups of $C_{\infty h}$, C_{1h}, C_{2h}, C_{3h}, C_{4h}, C_{5h}, and C_{6h}, respectively. (c) SEM images of fabricated TA-CGSMs belonging to belonging to cyclic groups of $C_{\infty h}$ and C_{1h} with scale bars of 1 μm. (d) Experimental setup for a spin-dependent beam separation measurement. (e,f) Far-field intensity distributions scattered from TA-CGSM belonging to cyclic groups of $C_{\infty h}$, C_{1h}, C_{2h}, C_{3h}, C_{4h}, C_{5h}, and C_{6h} for I_{-+} and I_{+-}, respectively, measured with λ = 1310 nm incidence Gaussian beam. (g) Plot of the intensity difference $\Delta I = I_{-+} - I_{+-}$.

4.2 Sample fabrication and experimental result of spin-dependent beam profile measurements

In Figure 3 (a) are shown schematics of TA-CSGM, where each TA-CSGM is composed of multiple TA nano-rods with varying width d from 45 nm to 150 nm placed in eight azimuthal segments of concentric rings repeated with 600 nm radial spacing. Figure 3 (b) shows optical microscope images of the fabricated TA-CGSMs belonging to cyclic groups of $C_{\infty h}$, C_{1h}, C_{2h}, C_{3h}, C_{4h}, C_{5h}, and C_{6h}, and SEM images of $C_{\infty h}$ and C_{1h} TA-CGSMs are shown in Figure 3 (c). For CPL beam source, we adopted a single mode fiber pigtailed laser diode (1310 nm) with output fiber diameter 50 μm. In Figure 3 (d), P is polarizer and LCVR is a liquid-crystal variable retarder.

Experimental measurement of spin-dependent beam separation is performed at a propagating distance of $D = 50\,\text{mm}$, which gives the transverse shift of $\Delta = 2 \times 0.02 \times \sigma \times D = 2\,\text{mm}$ for 1310 nm incidence beam wavelength. First of all, the vortex charge of cross-polarization scattering beam from $C_{\infty h}$ TA-CGSM is identified by an interference pattern between scattering vortex and incidence Gaussian beams. Counter-clockwise and clockwise twisted fringes confirmed topological charges of $l = 2$ and $l = -2$ of I_{-+} and I_{+-}, respectively. See Figure S1 of Supplementary Information.

Cross-polarization scattering beam profiles are displayed in Figure 3 (e) and (f). $C_{\infty h}$ TA-CGSM exhibits degenerate ϕ-independent intensity profiles for I_{-+} and I_{+-} as displayed in Figure 1 (f) and (g). On the other hand, $C_{nh}(n \neq \infty)$ TA-CGSMs exhibits ϕ-dependent intensity profiles of I_{-+} and I_{+-}, namely, asymmetric helical wavefronts.

5 Discussion

5.1 Symmetry property of vortex beam profiles under σ_h and C_2

Far-field electric fields of asymmetric vortex beams shown in Figure 3 (e) and (f) can be described as below.

$$E(r, \phi)_{-+} = A(r, \phi)\exp\{i\Phi_{tot}^{-+}(\phi)\}$$
$$E(r, \phi)_{+-} = B(r, \phi)\exp\{i\Phi_{tot}^{+-}(\phi)\} \quad (2)$$

where the azimuthal gradient of $\Phi_{tot}(\phi)$, $\nabla_\phi\Phi_{tot}(\phi)$, is ϕ-dependent.

Regarding $\Phi_{tot}^{-+}(\phi)$ and $\Phi_{tot}^{+-}(\phi)$, we note that the spiral trajectory for $\{+-\}$ is the mirror image of that for $\{-+\}$ with the equator plane of Poincaré sphere as a mirror plane, i.e., the senses of rotation are opposite to each other. This leads to the relation of total phases $\Phi_{tot}^{-+}(\phi) = -\Phi_{tot}^{+-}(\phi)$, the same in magnitude but opposite in sign. See Figure 4 (d), (e), (D), and (E). Furthermore, since C_{nh} TA-CGMS is invariant under σ_h operation, scattering amplitude of $\{-+\}$ from C_{nh} TA-CGM is the same as that of $\{+-\}$ from π-rotated TA-CGM, i.e., $E(r, \phi)_{-+} = E(r, \phi + \pi)_{+-}$. Accordingly, we obtain the relation of $I_{-+}(\phi) = I_{+-}(\phi + \pi)$ between scattering intensities of $\{-+\}$ and $\{+-\}$. See Figure 3 (e) and (f) and Figure 4 (a), (b), (A), and (B). This is true for C_{nh} (both even and odd n) TA-CGSMs.

On the other hand, C_{nh} (even n) TA-CGSMs is invariant under a simultaneous operations of σ_h and i, which is equivalent to the invariance of C_{nh} (even n) TA-CGSMs under C_2 operation. That is, scattering amplitude from C_{nh} (even n) TA-CGSM is the same as that from π-rotated C_{nh} (even n) TA-CGSM. In other words, $I_{+-}(\phi + \pi) = I_{+-}(\phi)$ and $I_{-+}(\phi + \pi) = I_{-+}(\phi)$. Combining with the above relation $I_{-+}(\phi) = I_{+-}(\phi + \pi)$, we obtain $I_{-+}(\phi) = I_{+-}(\phi)$, which leads to that $\Delta I = I_{-+} - I_{+-}$ is null for C_{nh} (even n) TA-CGSMs, but not for C_{nh} (odd n) TA-CGSMs. See the plot of $\Delta I = I_{-+} - I_{+-}$ in Figure 3, similar to what is reported in Ref [24].

5.2 Partial-wave expansion and azimuthal interference pattern

5.2.1 Partial-wave expansion

TA-CGSM renders azimuthal gradient $\nabla_\phi\Phi_{tot}$ of cross-polarization scattering beam to be ϕ-dependent, leading to ϕ-dependent helical wavefront, equivalently, to ϕ-dependent scattering amplitude in far-field as shown in experimental measurements of Figure 3 (e) and (f). This indicates that the scattering amplitude is composed of vortex beams of topological charge not only $l = 2$ but also $l \neq 2$.

Bessel-Gaussian (BG) beam satisfies a paraxial equation of propagation and it describes an azimuthal symmetric intensity distribution carrying orbital angular momentum. [25] We note two properties of BG beams relevant to the spatial beam profiles observed in our experiment for a series of TA-CGSMs. The first property is that BG beams can be built up by a superposition of decentered Gaussian beams, whose centers are positioned on a circle and the beam direction of which points to the apex of a cone. [26] This is related to $C_{\infty h}$ TA-CGSM, where the azimuthal symmetric annular beam intensity results from a superposition of decentered Gaussian beams scattered from each plasmonic segment of $C_{\infty h}$ TA-CGSM. The second property is that an asymmetric Bessel-Gaussian beam can be represented as a linear combination of symmetric Bessel-Gaussian beams. [25] This is related to C_{1h}, C_{2h}, C_{3h}, C_{4h}, C_{5h}, and C_{6h} TA-CGSMs, where the spatial beam profile has an annular shape possessing azimuthal angle depenedent intensity distribution.

Since C_{1h}, C_{2h}, C_{3h}, C_{4h}, C_{5h}, and C_{6h} TA-CGSMs are of a ring structure with cyclic group symmetry lowered from that of $C_{\infty h}$ TA-CGSM, we adopt BG beams as basis in a partial-wave expansion to examine how the symmetry lowering of azimuthal distribution of nano-rods modifes BG beam profile of the scattering light from azimuthal symmetric $C_{\infty h}$TA-CGSM. Vortex beam of topological charge l is described by the lth order Bessel-Gaussian beam $BG_l(r)e^{il\phi}$, [27]

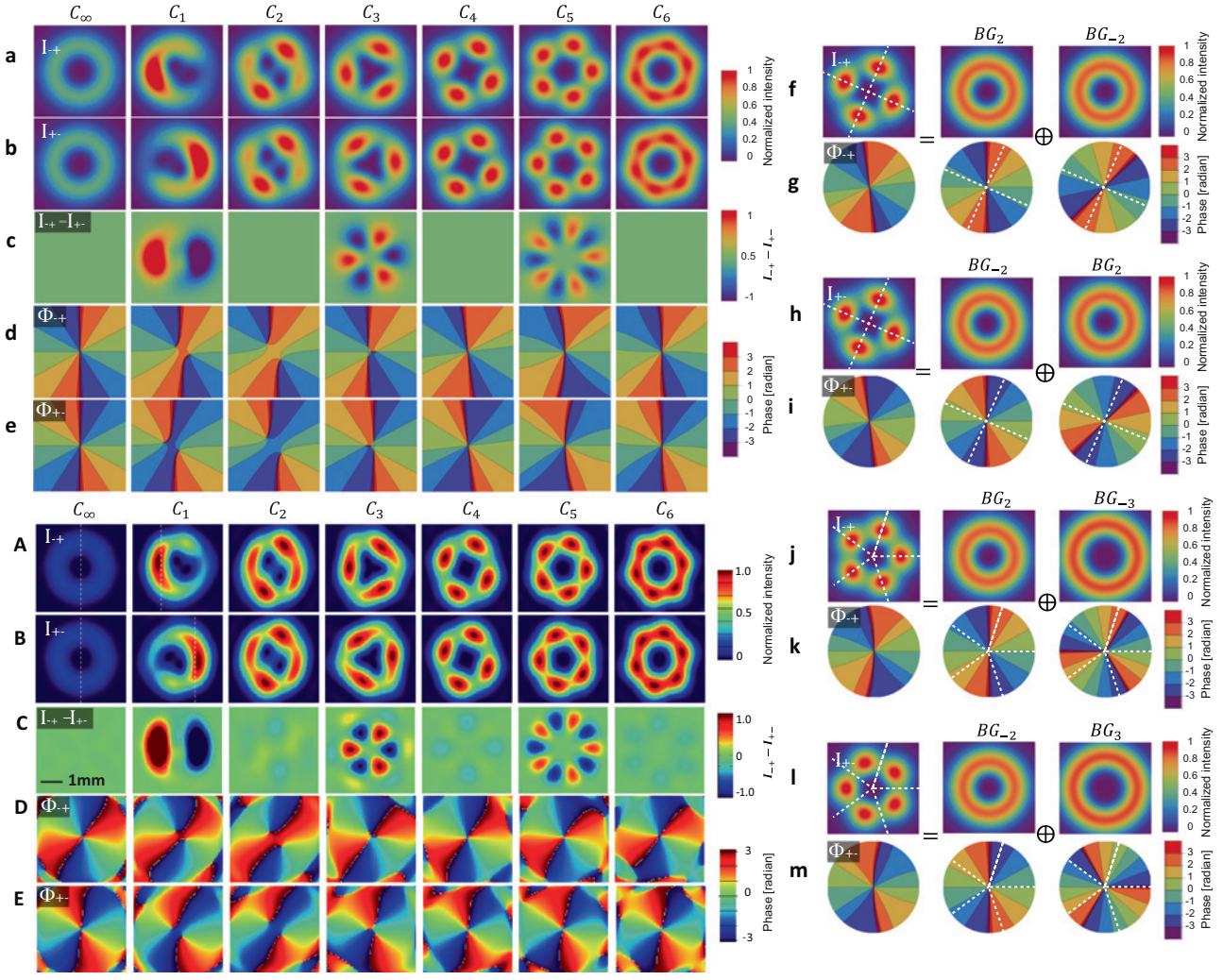


Figure 4: Analytical calculation and FDTD calculation of a spin-dependent beam separation for TA-CGSM. (a, b) Analytically calculated far-field intensity of I_{-+} and I_{+-}, respectively. (c) Calculated $\Delta I = I_{-+} - I_{+-}$. (d, e) Azimuthal distribution of phase for $C_{\infty h}$, C_{1h}, C_{2h}, C_{3h}, C_{4h}, C_{5h}, and C_{6h} TA-CGSM. (f-i) Partial-wave expansion of E_{-+} and E_{+-} of C_{4h} CGSM. (A, B) FDTD calculated far-field intensity of I_{-+} and I_{+-}, respectively. (C) Calculated $\Delta I = I_{-+} - I_{+-}$. (D, E) Azimuthal distribution of phase for $C_{\infty h}$, C_{1h}, C_{2h}, C_{3h}, C_{4h}, C_{5h}, and C_{6h} TA-CGSM. (j-m) Partial-wave expansion of E_{-+} and E_{+-} of C_{5h} CGSM.

$$BG_l(r)e^{il\phi} = J_l(k_0 r)e^{-k_0^2 r^2}e^{il\phi}$$

where nth order Bessel function $J_n(x)$ satisfies a symmetry relation $J_{-n}(x) = (-1)^n J_n(x)$. Now we express ϕ-dependent scattering amplitude as a linear combination of Bessel-Gaussian beams with partial-wave expansion coefficient $\tilde{a}_l$[25, 28].

$$E(r, \phi)_{-+} = A(r, \phi)e^{i\Phi_{tot}^{-+}(\phi)} = \sum_l \tilde{a}_l BG_l(r)e^{il\phi} \tag{3}$$

$$\tilde{a}_l \equiv a_l e^{i\psi_l} \tag{4}$$

where $\tilde{a}_l$ is the lth order expansion coefficient of Fourier expansion, $A(r, \phi) = |E(r, \phi)|$ is the amplitude, and $\Phi_{tot} = \Phi_{PB} + \Phi_D = \tan^{-1}[\mathrm{Im}(E)/\mathrm{Re}(E)]$ is the total phase.

When the second term $\Phi_D(\phi)$ of (1) is absent, the azimuthal gradient $\nabla_\phi \Phi_{tot}$ reduces to +2, generating a vortex beam of topological charge +2. That is, $\tilde{a}_2 = 1$ and $\tilde{a}_l = 0$ for $l \neq 2$ in (3). The presence of $\Phi_D(\phi)$ of (1) is responsible for additional generation of vortex beams of topological charge $l \neq 2$, and magnitude a_l and phase ψ_l of $\tilde{a}_l$ $(l \neq 2)$ in (4) describes how additional vortex beams contribute to determining ϕ-dependence of scattering amplitude.

Vortex beam profile, i. e., far-field intensity, $I_{-+}(r, \phi) = |E(r, \phi)_{-+}|^2$, is nothing but the interference pattern between vortex beam of $l = 2$ and additional vortex beams of $l \neq 2$, originating from non-constant azimuthal gradient $\nabla_\phi \Phi_{tot}$. While magnitude a_l is a measure of contribution of

vortex beam of $l \neq 2$, phase ψ_l plays an important role in determining azimuthal distribution of intensity $I_{-+}(r, \phi)$, that is, the azimuthal location of bright and dark spots observed in vortex beams. An expression similar to (3) holds for $E(r, \phi)_{+-}$ with $\Phi_{tot}^{-+}(\phi) = -\Phi_{tot}^{+-}(\phi)$ in (2) as discussed in Section 5.1.

The partial-wave expansion analysis was adopted to relate group order n of cyclic symmetry in the interference pattern of the partial waves and spin-dependent beam splitting. By employing (3) and (4), i. e., $I(r, \phi)_{-+} = \left|E(r, \phi)_{-+}\right|^2 = \left|\sum_l \tilde{a}_l BG_l(r)e^{il\phi}\right|^2$, the partial-wave expansion coefficient $\tilde{a}_l \equiv a_l e^{i\psi_l}$ is obtained by a least-squared-fit of the experimentally measured intensity profiles I_{-+} as a function of azimuthal angle in Figure 3 (e) & (f), and the fitted intensity and phase of scattered fields are plotted in Figure 4 (a) & (b) and (d) & (e), respectively. The fit values of magnitude a_l and phase ψ_l of $\tilde{a}_l$ in (4) are listed in Figure 5 (g).

5.2.2 Azimuthal interference pattern and correlation between group order n of C_{nh} and topological charge l

Now we study the interference behavior between $l = +2$ ($l = -2$) and partial-wave vortex beams having difference topological charge $l \neq +2$ ($l \neq -2$) for {−+} ({+−}) scattering originating from ϕ-dependent$\nabla_\phi \Phi_D(\phi)$.

In order to identify the correlation between additionally generated vortex beam of topological charge l and group order n of C_{nh}, we consider {−+} scattering where vortex beam of $l = 2$ and additional vortex beam of $l \neq 2$ interfere each other. From (3) we have

$$E(r, \phi)_{-+} = A(r, \phi)e^{i\Phi_{PB}^{+}(\phi)} = BG_2(r)e^{i2\phi} + a_l e^{i\psi_l} BG_l(r)e^{il\phi}$$

$$= e^{i2\phi}\left[BG_2(r) + a_l BG_l(r)e^{i(l+2)\phi + l\psi_l}\right], (l \neq 2) \quad (5)$$

In (5) the amplitude $A(r, \phi)$ is expressed as below.

$$A(r, \phi) = \left[2a_l BG_2(r)BG_l(r)\cos\{(l+2)\phi + l\psi_l\}\right.$$

$$\left. + BG_2(r)^2 + a_l^2 BG_l(r)^2\right]^{\frac{1}{2}} \quad (6)$$

Azimuthal angle dependence is described by the first term of (6), which is the interference term. As azimuthal angle ϕ increases from 0 to 2π, a constructive interference takes place at azimuthal angle $\phi_m = m \cdot \phi_0$ (m = integer) with ϕ_0 satisfying the relation $(l+2)\phi_0 = 2\pi$. That is, there are $l+2$ numbers of bright spots at the intensity $I_{-+}(r, \phi)$ of vortex beam with asymmetric helical wavefront. On the other hand, the interference should possess n-fold rotation symmetry dictated by group order n of C_{nh}. Therefore we have the relation between l and n as n = $l + 2$ or

$$l = 2 - n \quad (7)$$

By looking up the table listed in Figure 5 (g) we find that the relation of (7) holds for all C_{nh} TA-CGSMs. Note that the non-vanishing vortex beams of $l = -1$ for C_{1h} and $l = -2$ for C_{2h} have the helicity opposite to that of generated vortex beams of $l = +1$ for C_{1h} and $l = +2$ for C_{2h}, and the interference term of two vortex beams of opposite helicities $+l$ and $-l$ is not ϕ-dependent as can be seen easily in (5) when $\tilde{a}_{-l}$ is added.

Partial wave expansions with fit values listed in Figure 5 (g) are explicitly expressed as below for C_{4h} TA-CGSM,

$$E(r, \phi)_{-+} = BG_2(r)e^{+i2\phi} + 0.24BG_{-2}(r)e^{-i2\phi}\exp\left(+i\frac{3\pi}{2}\right)$$

$$= BG_2(r)e^{+i2\phi} - i0.24BG_2(r)e^{-i2\phi}, \quad (8)$$

$$E(r, \phi)_{+-} = BG_{-2}(r)e^{-i2\phi} + 0.24BG_2(r)e^{+i2\phi}\exp\left(-i\frac{3\pi}{2}\right)$$

$$= BG_2(r)e^{-i2\phi} + i0.24BG_2(r)e^{+i2\phi}, \quad (9)$$

and for C_{5h} TA-CGSM,

$$E(r, \phi)_{-+} = BG_2(r)e^{+i2\phi} + BG_{-3}(r)e^{-i3\phi}\exp(+i\pi)$$

$$= BG_2(r)e^{+i2\phi} - BG_3(r)e^{-i3\phi}\exp(+i\pi)$$

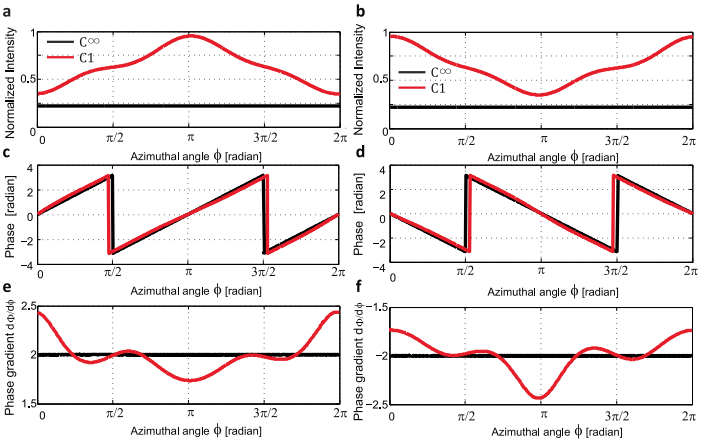
$$= BG_2(r)e^{+i2\phi} + BG_3(r)e^{-i3\phi}, \quad (10)$$

$$E(r, \phi)_{+-} = BG_{-2}(r)e^{-i2\phi} + BG_3(r)e^{+i3\phi}\exp(-i\pi)$$

$$= BG_2(r)e^{-i2\phi} - BG_3(r)e^{+i3\phi}. \quad (11)$$

From Eqs. (9)–(10) the intensity and phase of the sum of $l = \pm 2$ vortex and partial-wave vortex beams are plotted for {−+} ({+−}) scattering in C_{4h} TA-CGSM and C_{5h} TA-CGSM as displayed in Figure 4 (f) & (g) (Figure 4 (h) & (i)) and Figure 4 (j) & (k) (Figure 4 (l) & (m)), respectively. We find that $\Delta I = I_{-+} - I_{+-} = 0$ for C_{4h} and $\Delta I \neq 0$ for C_{5h} TA-CGSMs.

We also adopted finite difference time domain (Lumerical FDTD) method to calculate the far-field intensity (I_{-+}, I_{+-}) and phase (Φ_{-+}, Φ_{+-}) distributions of scattered field from C_{nh} metasurfaces. See Figure 4 (A-E) for FDTD calculation, which is in a perfect agreement with experimental results.



g

		E_{-+}							E_{+-}						
	l	-4	-3	-2	-1	0	1	2	-2	-1	0	1	2	3	4
C_1	a_l	0	0	0	0.02	0.01	0.1	1	1	0.1	0.01	0.02	0	0	0
	ψ_l	0	0	0	0	$\pi/2$	π	0	0	$-\pi$	$-\pi/2$	0	0	0	0
C_2	a_l	0	0	0.12	0	0.02	0	1	1	0	0.02	0	0.12	0	0
	ψ_l	0	0	$3\pi/2$	0	$\pi/2$	0	0	0	0	$-\pi/2$	0	$-3\pi/2$	0	0
C_3	a_l	0	0	0	0.05	0	0	1	1	0	0	0.05	0	0	0
	ψ_l	0	0	0	0	0	0	0	0	0	0	0	0	0	0
C_4	a_l	0	0	0.24	0	0	0	1	1	0	0	0	0.24	0	0
	ψ_l	0	0	$3\pi/2$	0	0	0	0	0	0	0	0	$-3\pi/2$	0	0
C_5	a_l	0	1	0	0	0	0	1	1	0	0	0	0	1	0
	ψ_l	0	π	0	0	0	0	0	0	0	0	0	0	$-\pi$	0
C_6	a_l	1.74	0	0	0	0	0	1	1	0	0	0	0	0	1.74
	ψ_l	$\pi/2$	0	0	0	0	0	0	0	0	0	0	0	0	$-\pi/2$

Figure 5: Analytically calculated intensity, phase, and phase gradient as a function of the azimuthal angle ϕ. (a, b) Calculated far-field intensity I_{ij}. (c, d) Calculated phase Φ_{ij}. (e,f) constant phase gradient $d\Phi_{ij}/d\varphi$ of $C_{\infty h}$ (black) and nonuniform phase gradient of C_{1h} (red). The plots are for $\{ij\}$ configuration, where $\{ij\}$ are detection and incidence circular polarization helicity, $\{-+\}$ for (a, c, e) and $\{+-\}$ for (b, d, f). Non-constant phase gradient takes place owing to ϕ-dependent $\nabla_\phi \Phi_D(\phi)$. (g) Fit values of partial-wave expansion coefficient $\tilde{a}_l$, the lth order expansion coefficient.

5.3 Non-constant azimuthal gradient of total phase

Now we identify how non-constant azimuthal gradient of dynamical phase is related to the vortex beam profile, in particular, the distribution of bright and dark spots. As discussed in Section 3, a destructive interference takes place between cross-polarization scatterings from the long- and short-axis excitations. Differently from the long-axis excitation scattering, the short-axis excitation scattering is ϕ-dependent for C_{nh} TA-CGSM, leading to ϕ-dependent interference, which is associated with ϕ-dependent $(\nabla_\phi \Phi_D(\phi))$ in (1) as illustrated in Figure (2) (b).

From the view point of wavefront manipulation by a local phase control through metasurface, the presence of ϕ-dependent $\nabla_\phi \Phi_D(\phi)$ at C_{nh} TA-CGSM alters the wavefront along the azimuthal direction. To elucidate how a phase gradient across a propagating beam cross-section alters wavefront, let's consider a simple circular convex lens converging an incident beam toward the center, where dynamical phase Φ_D is responsible for refraction.

Along a straight line drawn from one point at the circumference of circular convex lens passing through the center to the other opposite point, linear gradient of dynamical phase, $\nabla\Phi_D$, changes sign from positive to negative when crossing the center, where the magnitude of $\nabla\Phi_D$ being the minimum as zero. That is, the alteration of wavefront is minimum at the point having the minimum $|\nabla\Phi_D|$ across beam cross-section, leading to converging of the incident beam toward the center.

In a similar way, azimuthal gradient of total phase is modulated around the value $\nabla_\phi \Phi_{PB} = +2\ (-2)$ owing to the presence of ϕ-dependent $\nabla_\phi \Phi_D$, subsequently resulting in an azimuthal alteration of wavefront. In C_{1h} TA-CGSM, for example, the minimum $\left|\nabla_\phi \Phi_{tot}^{-+}\right|$ $(\left|\nabla_\phi \Phi_{tot}^{+-}\right|)$ takes place at near $\phi = \pi$ $(\phi = 0 \equiv 2\pi)$ at $\lambda = 1300\,\text{nm}$, leading to converging of the incident beam along the azimuthal direction toward the angle near $\phi = \pi$ $(\phi = 0 \equiv 2\pi)$ of the single bright spot. Dependence of scattering intensity and phase gradient on azimuthal angle ϕ is compared in Figure 5. See Figure 5 (e) and Figure 5 (f) for $\{-+\}$ and $\{+-\}$ scatterings, respectively. The number of bright spots is equal to the number of the local minimum $\left|\nabla_\phi \Phi_{tot}\right|$ in both $\{-+\}$ and $\{+-\}$ scatterings.

We note that the symmetry dictated by σ_h operation leads to $I_{-+}(\phi) = I_{+-}(\phi + \pi)$ as discussed in Section 5.1. In fact, the coincidence of angular locations of a bright spot and a local minimum of $\left|\nabla_\phi \Phi_{tot}\right|$ is evident as seen in the plot of Figure 5 (a) and (c). Refer to Figure 2 of Supplementary Information for C_{nh} TA-CGSMs $(n \neq 1)$.

In fact, the azimuthal distribution of bright and dark spots and radial node lines in cross-scattering intensity results from interplay of ϕ-independent $\nabla_\phi \Phi_{PB}$ and ϕ-dependent$\nabla_\phi \Phi_D$. In other words, the original helical wavefronts with the azimuthal geometric phase gradient ±2 are altered by an introduction of non-constant azimuthal gradient $\nabla_\phi \Phi_D$, to focus wavefront along azimuthal direction to build a bright spot, similar to focusing wavefront along radial direction by optical antenna metasurface in flat optics. [6–10]

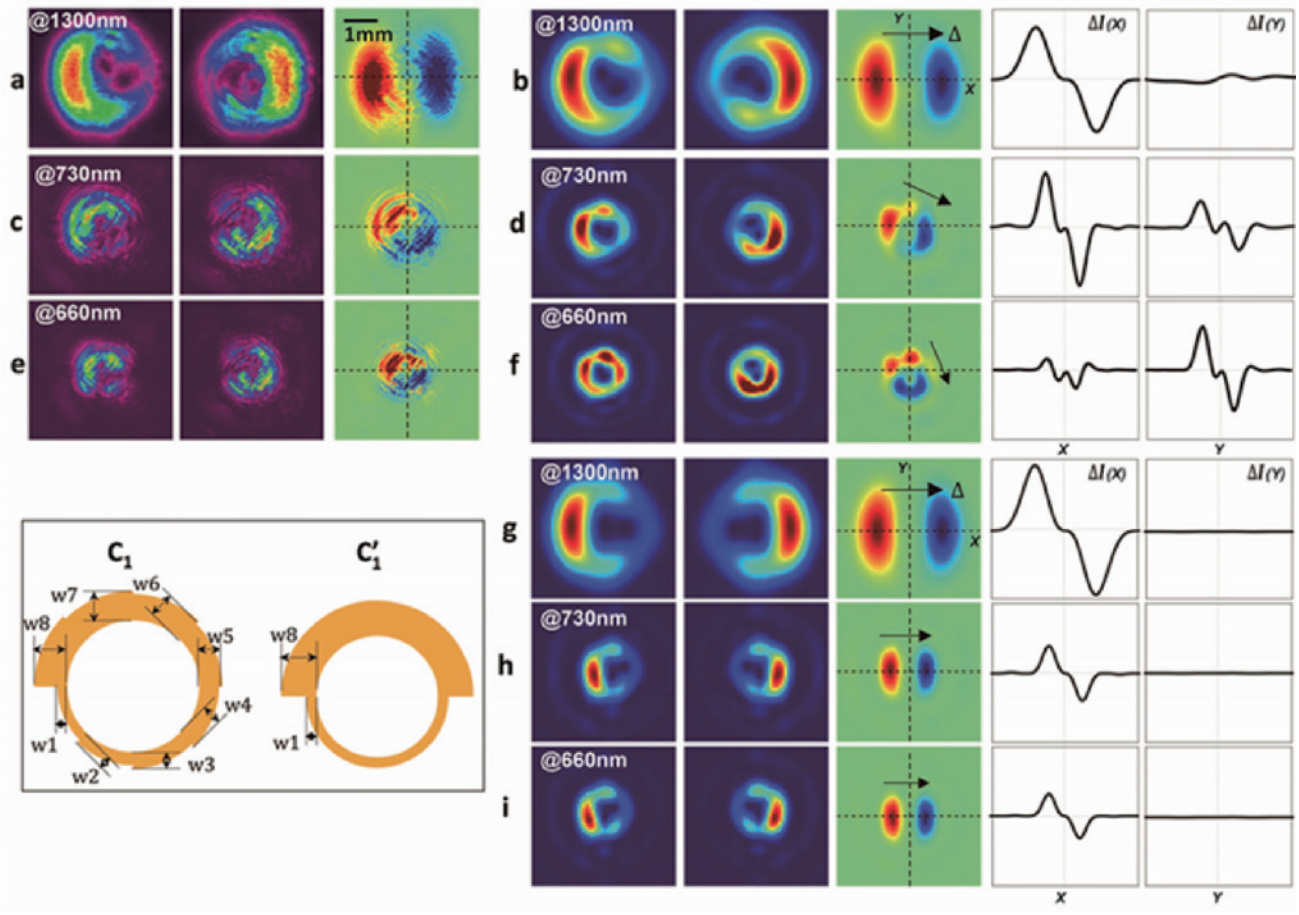


Figure 6: Wavelength-dependence of a spin-dependent beam separation. Wavelength-dependence of a spin-dependent beam separation in C_{1h} TA-CGSM metasurface is shown at 1300 nm, 730 nm, and 660 nm. (a), (c), (e), Experimental measurements and (b), (d), (f), FDTD calculations for C_{1h} TA-CGSM. g,h,i, FDTD calculations for C_{1h}' metasurface with incident Gaussian beam propagation along $+\hat{z}$.

5.4 Wavelength dependence of spin-dependent beam separation

As noted in Section 3, there occurs a destructive interference between scatterings from the long- and short-axis excitations, which is responsible for vortex beam profiles when cross-polarization scattered from for C_{nh} TA-CGSMs. In a given C_{nh} TA-CGSM, TA has a varying width with the same fixed length, and scattering amplitude from plasmonic excitation along short-axis of the varying width depends on plasmonic resonance. This leads to that the spin-dependent beam separation in vortex beam generation depends on wavelength of incident Gaussian beam.

We performed experimental measurement of spin-dependent beam separation of C_{1h} TA-CGSM by employing lasers with different wavelengths. Single-mode fiber pigtailed laser diodes with wavelengths $\lambda = 1310\,\text{nm}$, $\lambda = 730\,\text{nm}$, and $\lambda = 660\,\text{nm}$ are adopted as normal-incidence Gaussian beam sources. Azimuthal interference pattern goes through clock-wise rotation as wavelength gets shorter as shown in beam profile measurement and FDTD simulation at the top panel of Figure 6.

It is known that geometric phase is non-dispersive. However, scattering amplitude from short-axis excitation depends on the relative spectral location of incident beam wavelength with respect to plasmonics resonance. Subsequently, the location of polarization state at Poincaré sphere depends on the incident beam wavelength. As a result, non-constant azimuthal gradient $\nabla_\phi \Phi_D$ is dispersive.

In order to confirm that dispersive $\nabla_\phi \Phi_D$ is responsible for wavelength-dependent azimuthal interference pattern from C_{1h} TA-CGSM, we examined C_1' metasurface composed of two semicircles with different thicknesses as shown at bottom-left panel of Figure 6, which possesses σ_{yz} symmetry, i. e., reflection symmetry with respect to yz-plane. FDTD simulation of cross-polarization scattering shows that spin-dependent vortex beam separation

Table 1: Table of lth order expansion coefficient for $\lambda = 1300$ nm.

$\lambda = 1300$ nm		E_{-+}					E_{+-}				
l		−2	−1	0	1	2	−2	−1	0	1	2
C_1	a_l	0	0.02	0.01	0.1	1	1	0.1	0.01	0.02	0
	ψ_l	0	0	$\pi/2$	π	0	0	$-\pi$	$-\pi/2$	0	0
C_1'	a_l	0	0.02	0	0.1	1	1	0.1	0	0.02	0
	ψ_l	0	0	0	π	0	0	$-\pi$	0	0	0

takes place always along x-direction for all three different wavelengths as shown at the bottom panel of Figure 6. Scattering from one semi-circle results in one full circle of polarization states in Poincaré sphere, and thereby introduces 2π of PB phase for each semi-circle as discussed in Section 2. However, the difference in thickness of two semi-circles results in $\nabla_\phi \Phi_D \neq \pm 2$ at $\phi = 0\,\&\,\pi$, regardless of incident beam wavelength. As a result, a vortex beam with asymmetric wavefront is generated, which is composed of vortex beams of $l = \pm 2$ and $l = \pm 1$ as shown in Tables 1, 2, and 3.

A careful examination of the bottom panel of Figure 6 shows that there occurs a beam deflection in vertical direction along with spin-dependent vortex beam separation in horizontal direction. This is an example of beam deflection according to generalized Snell's law.[29, 30] That is, the existence of $\nabla_\phi \Phi_D$ along y-direction is equivalent to the presence of phase discontinuity along y-direction, giving rise to $\delta\vec{k}$ in linear momentum $\vec{k}$ of scattered vortex beam along y-direction, and a vertical deflection of vortex beam takes place, which is wavelength-dependent. In C_1' metasurface, the minimum $|\nabla_\phi \Phi_{tot}^{-+}|$ ($|\nabla_\phi \Phi_{tot}^{+-}|$) takes place at $\phi = \pi$ ($\phi = 0 \equiv 2\pi$). Owing to σ_{yz} symmetry, the net gradient of $\hat{\phi}$-dependent $\nabla_\phi \Phi_{tot}$ is located at $\phi = \pi$ or $\phi = 0 \equiv 2\pi$ with direction along $\hat{\phi}$ corresponding to $-y$ direction for both $\{-+\}$ and $\{+-\}$ scatterings, which leads to $\delta < \vec{p} >$ along $-\hat{y}$.

Consequently, photonic spin Hall effect takes place as a spin-dependent separation of vortex beam in horizontal direction. Berry curvature is the topological magnetic monopole, $\vec{B}(\vec{p}) = \hat{p}/p^2$, and Lorentz equation of motion in momentum space is $\delta\vec{x} = \sigma\delta\vec{p} \times \vec{B}(p)$. In helical wavefront, mean momentum $<\vec{p}>$ is along the vortex beam propagation direction and takes part in Lorentz equation of motion, i. e., $\delta < \vec{x} > = \sigma\delta < \vec{p} > \times \vec{B}(< \vec{p} >)$. Hence, the transverse shift owing to photonic spin Hall effect takes place in $-\hat{x}$ and $+\hat{x}$ directions for incident LCP ($\sigma = +1$) and RCP ($\sigma = -1$) Gaussian beams, respectively, as displayed in the bottom panel of Figure 6.[31, 32] The interpretation of spin-dependent beam separation for C_{nh} in terms of photonic spin Hall effect is not straightforward due the difficulty in identifying the net gradient of $\hat{\phi}$-dependent $\nabla_\phi \Phi_{tot}$.

Normalized horizontal (X) and vertical (Y) spin-dependent beam separation profiles, ΔI(X) and ΔI(Y) along the dashed coordinate axes, are displayed in two right panels, where $\Delta I = I_{-+}(r, \phi) - I_{+-}(r, \phi)$.

6 Conclusion

Tapered arc cyclic group symmetric metasurface is introduced to explore the details of optical spin-dependent beam separation in spin-to-orbital angular momentum conversion. Presence of non-constant azimuthal gradient of total phase is found to be responsible for azimuthal interference pattern in vortex beams with asymmetric helical wavefront. By identifying the role of non-constant azimuthal gradient of total phase in giving rise to spin-dependent beam separation, spatial separation and vortex beam profiling are achieved in a controllable manner.

Table 2: Table of lth order expansion coefficient for $\lambda = 730$ nm.

$\lambda = 730$ nm		E_{-+}					E_{+-}				
l		−2	−1	0	1	2	−2	−1	0	1	2
C_1	a_l	0	0.02	0.01	0.1	1	1	0.1	0.01	0.02	0
	ψ_l	0	$-\pi/5$	$3\pi/10$	$4\pi/5$	0	0	$-4\pi/5$	$-3\pi/10$	$\pi/5$	0
C_1'	a_l	0	0.02	0	0.1	1	1	0.1	0	0.02	0
	ψ_l	0	$\pi/5$	0	π	0	0	$-\pi$	0	$-\pi/5$	0

Table 3: Table of lth order expansion coefficient for $\lambda = 660$ nm.

λ = 660 nm		E_{-+}					E_{+-}				
l		−2	−1	0	1	2	−2	−1	0	1	2
C_1	a_l	0	0.02	0.01	0.1	1	1	0.1	0.01	0.02	0
	ψ_l	0	$-2\pi/5$	$\pi/10$	$3\pi/5$	0	0	$-3\pi/5$	$-\pi/10$	$2\pi/5$	0
$C_1^{'}$	a_l	0	0.02	0	0.1	1	1	0.1	0	0.02	0
	ψ_l	0	$\pi/5$	0	$11\pi/10$	0	0	$-11\pi/10$	0	$-\pi/5$	0

Azimuthal interference pattern in vortex beams with asymmetric helical wavefront found to be related to symmetry property of cyclic group C_{nh}, and group order n determines topological charge $l \neq \pm 2$ of additional vortex beams. Our work enhances a fundamental understating of interplay between spin- and orbital angular momentum of light in metasurface. Also our finding provides a significant advantage in applications such as vortex multiplexing in optical communication and optical tweezers employing vortex beams.

Acknowledgments: JWW acknowledges the support from the Ministry of Science, ICT & Future Planning, Korea (2017R1E1A1A01075394, 2014M3A6B3063706). Nanofabrication processes were performed in PLANETE cleanroom facility, CT PACA.

Author contribution: All the authors have accepted responsibility for the entire content of this submitted manuscript and approved submission.

Research funding: None declared.

Employment or leadership: None declared.

Honorarium: None declared.

Conflict of interest statement: The authors declare no conflicts of interest regarding this article.

References

[1] Z. Bomzon, V. Kleiner, and E Hasman, "Pancharatnam–berry phase in space-variant polarization-state manipulations with subwavelength gratings," *Optics Lett.*, vol. 26, no. 18, pp. 1424–1426, 2001.

[2] Z. Bomzon, G. Biener, V. Kleiner, and E. Hasman, "Space-variant pancharatnam–berry phase optical elements with computer-generated subwavelength gratings," *Optics Lett.*, vol. 27, no. 13, pp. 1141–1143, 2002.

[3] G. Biener, A. Niv, V. Kleiner, and E. Hasman, "Formation of helical beams by use of pancharatnam–berry phase optical elements," *Optics Lett.*, vol. 27, no. 21, pp. 1875–1877, 2002.

[4] K. Y Bliokh, A. Niv, V. Kleiner, and E. Hasman, "Geometrodynamics of spinning light," *Nat. Photon.*, vol. 2, no. 12, p. 748, 2008.

[5] N. Shitrit, I. Yulevich, E. Maguid, et al., "Spin-optical metamaterial route to spin-controlled photonics," *Science*, vol. 340, no. 6133, pp. 724–726, 2013.

[6] N. Yu, P. Genevet, F. Aieta, et al., "Flat optics: controlling wavefronts with optical antenna metasurfaces," *IEEE J. Sel. Top. Quant. Electron.*, vol. 19, no. 3, p. 4700423, 2013.

[7] N. Yu and F. Capasso, "Flat optics with designer metasurfaces," *Nat. Mater.*, vol. 13, no. 2, pp. 139, 2014.

[8] M. Khorasaninejad, W. T. Chen, R. C Devlin, J. Oh, A. Y. Zhu, and F. Capasso, "Metalenses at visible wavelengths: Diffraction-limited focusing and subwavelength resolution imaging," *Science*, vol. 352, no. 6290, pp. 1190–1194, 2016.

[9] M. Jiang, Z. N. Chen, Y. Zhang, W. Hong, and X. Xuan, "Metamaterial-based thin planar lens antenna for spatial beamforming and multibeam massive mimo," *IEEE Trans. Antenn. Propag.*, vol. 65, no. 2, pp. 464–472, 2016.

[10] F. Capasso, "The future and promise of flat optics: a personal perspective," *Nanophotonics*, vol. 7, no. 6, pp. 953–957, 2018.

[11] L. Marrucci, C. Manzo, and D. Paparo, "Optical spin-to-orbital angular momentum conversion in inhomogeneous anisotropic media," *Phys. Rev. Lett.*, vol. 96, no. 16, pp. 163905, 2006.

[12] L. Marrucci, E. Karimi, S. Slussarenko, et al., "Spin-to-orbital conversion of the angular momentum of light and its classical and quantum applications," *J. Optic.*, vol. 13, no. 6, p. 064001, 2011.

[13] E. Brasselet, Y. Izdebskaya, V. Shvedov, A. S. Desyatnikov, W. Krolikowski, and Y. S. Kivshar, "Dynamics of optical spin-orbit coupling in uniaxial crystals," *Optics Lett.*, vol. 34, no. 7, pp. 1021–1023, 2009.

[14] E. Brasselet, G. Gervinskas, G. Seniutinas, and S. Juodkazis, "Topological shaping of light by closed-path nanoslits," *Phys. Rev. Lett.*, vol. 111, no. 19, p. 193901, 2013.

[15] L. Zhu and J. Wang, "Arbitrary manipulation of spatial amplitude and phase using phase-only spatial light modulators," *Sci. Rep.*, vol. 4, p. 7441, 2014.

[16] E. Karimi, S. A. Schulz, I. De Leon, H. Qassim, J. Upham, and R. W. Boyd, "Generating optical orbital angular momentum at visible wavelengths using a plasmonic metasurface," *Light Sci. Appl.*, vol. 3, no. 5, p. e167, 2014.

[17] F. Bouchard, I. De Leon, S. A. Schulz, J. Upham, E. Karimi, and R. W. Boyd, "Optical spin-to-orbital angular momentum conversion in ultra-thin metasurfaces with arbitrary topological charges," *Appl. Phys. Lett.*, vol. 105, no. 10, p. 101905, 2014.

[18] J. Du and J. Wang, "Design of on-chip n-fold orbital angular momentum multicasting using v-shaped antenna array," *Sci. Rep.*, vol. 5, no. 1, pp. 1–5, 2015.

[19] C. I. Osorio, A. Mohtashami, and A. F. Koenderink, "K-space polarimetry of bullseye plasmon antennas," *Sci. Rep.*, vol. 5, p. 9966, 2015.
[20] R. C Devlin, A. Ambrosio, N. A. Rubin, J. B Mueller, and F. Capasso, "Arbitrary spin-to–orbital angular momentum conversion of light," *Science*, vol. 358, no. 6365, pp. 896–901, 2017.
[21] R. C. Devlin, A. Ambrosio, D. Wintz, et al., "Spin-to-orbital angular momentum conversion in dielectric metasurfaces," *Optics Express*, vol. 25, no. 1, pp. 377–393, 2017.
[22] K. Zhang, Y. Yuan, D. Zhang, et al., "Phase-engineered metalenses to generate converging and non-diffractive vortex beam carrying orbital angular momentum in microwave region," *Optics Express*, vol. 26, no. 2, pp. 1351–1360, 2018.
[23] H. T. Chen, A. J. Taylor, and N. Yu, "A review of metasurfaces: physics and applications," *Rep. Prog. Phys.*, vol. 79, no. 7, p. 076401, 2016.
[24] A. P. Slobozhanyuk, A. N. Poddubny, I. S. Sinev, et al., "Enhanced photonic spin hall effect with subwavelength topological edge states," *Laser Photon. Rev.*, vol. 10, no. 4, pp. 656–664, 2016.
[25] V. V. Kotlyar, A. A. Kovalev, R. V. Skidanov, and V. A. Soifer, "Asymmetric bessel–gauss beams," *J. Opt. Soc. Am. A*, vol. 31, no. 9, pp. 1977–1983, 2014.
[26] C. Palma, "Decentered gaussian beams, ray bundles, and bessel–gauss beams," *Appl. Optic.*, vol. 36, no. 6, pp. 1116–1120, 1997.
[27] J. Mendoza-Hernández, M. L. Arroyo-Carrasco, M. D. Iturbe-Castillo, and S. Chávez-Cerda, "Laguerre–gauss beams versus bessel beams showdown: peer comparison," *Optics Lett.*, vol. 40, no. 16, pp. 3739–3742, 2015.
[28] V. V. Kotlyar, A. A. Kovalev, and V. A. Soifer, "Asymmetric bessel modes," *Optics Lett.*, vol. 39, no. 8, pp. 2395–2398, 2014.
[29] N. Yu, P. Genevet, M. A. Kats, et al., "Light propagation with phase discontinuities: generalized laws of reflection and refraction," *science*, vol. 334, no. 6054, pp. 333–337, 2011.
[30] Y. U. Lee, J. Kim, J. H. Woo, et al., "Electro-optic switching in phase-discontinuity complementary metasurface twisted nematic cell," *Optics Express*, vol. 22, no. 17, pp. 20816–20827, 2014.
[31] X. Yin, Z. Ye, J. Rho, Y. Wang, and X. Zhang, "Photonic spin hall effect at metasurfaces," *Science*, vol. 339, no. 6126, pp. 1405–1407, 2013.
[32] Y. U. Lee and J. W. Wu, "Control of optical spin hall shift in phase-discontinuity metasurface by weak value measurement post-selection," *Sci. Rep.*, vol. 5, p. 13900, 2015.

Supplementary material: The online version of this article offers supplementary material (https://doi.org/10.1515/nanoph-2020-0160).